Biomedical Paper

Comparative *In Vitro* Study of Contact- and Image-Based Rigid Registration for Computer-Aided Surgery

Ofri Sadowsky, Ziv Yaniv, and Leo Joskowicz
Computer-Aided Surgery and Medical Image Processing Laboratory, School of Computer Science and Engineering, The Hebrew University of Jerusalem, Jerusalem, Israel

ABSTRACT
We present an *in vitro* study of rigid registration methods for computer-aided surgery. The goals of the study were to obtain accuracy measures empirically under optimal laboratory conditions, and to identify the weak links in the registration chain. Specifically, we investigated two common registration methods (contact-based registration and image-based landmark registration) and established a framework for comparing the accuracy of both methods. The phantoms, protocols, and algorithms for tool tip calibration, contact-based registration with an optical tracker, fluoroscopic X-ray camera calibration, and fluoroscopic X-ray image-based landmark registration are described. Average accuracies of 0.5 mm (1.5 mm maximum) and 2.75 mm (3.4 mm maximum) were found for contact-based and image-based landmark registration, respectively. Based on these findings, the camera calibration was identified as being the main source of error in image-based landmark registration. Protocol improvements and algorithmic refinements to improve the accuracy of image-based landmark registration are proposed.
Comp Aid Surg 7:223–236 (2002).

Key words: **registration; image-based registration; contact-based registration; accuracy measurements; fluoroscopy; tracking**

INTRODUCTION

Registration is the task of finding a transformation from the coordinate system of one modality data set to another so that all features appearing in one modality are aligned with their appearance in the second. Registration is an essential step in most computer-aided surgery (CAS) systems, because it is necessary to match information from different data modalities obtained at different points in time. It is required to match the preoperative images and plans to the intraoperative situation, and to determine the relative positions of surgical tools and anatomical structures. Examples of deployed CAS systems include preoperative planning, intraoperative navigation, and robotic systems for orthopedic surgery,[1–4] neurosurgery,[5,6] and maxillofacial surgery,[7] among many others. Practical, accurate, and robust registration has emerged as one of the key technical challenges in the field.[3] Much recent research has been devoted to the development and validation of registration methods (see ref. 8 for an excellent survey).

This article presents an *in vitro* study of rigid registration methods for CAS. The purpose of the study was to obtain accuracy measures empirically under optimal laboratory conditions and to identify

Received August 1, 2001; accepted May 9, 2002.

Address correspondence/reprint requests to: Prof. Leo Joskowicz, School of Computer Science and Engineering, The Hebrew University of Jerusalem, Givat Ram, Jerusalem 91904, Israel. E-mail: josko@cs.huji.ac.il

Published online in Wiley InterScience (www.interscience.wiley.com). DOI: 10.1002/igs.10048

the weak links in the registration chain. Although the setup was different from the one used clinically, the study aimed at obtaining a lower bound on the achievable accuracy, and at identifying the main sources of error. Establishing the accuracy and robustness of the registration methods is essential for determining their potential applicability in different clinical settings. Understanding of the factors that affect the accuracy and robustness of the registration process provides quantitative criteria to support the selection of registration methods, and indicates where technical improvements are necessary.

We addressed the rigid registration of the preoperative three-dimensional (3D) model of an object with its intraoperative pose. This type of registration is very common in orthopedics, where mesh models of bone structures are constructed preoperatively from CT scans, and a surgical plan, consisting of landmark points, axes, or implants, is elaborated based on the images and models. The plan must then be registered to the intraoperative situation so that it can be carried out precisely with the help of a navigation system or robotic device. The registration is usually performed by using an instrumented pointer to touch implanted fiducials, anatomical landmarks, or points on the surface of the anatomy to obtain their precise spatial locations. The points are then matched with the corresponding points in the 3D model to obtain the set of three rotation and three translation parameters of the rigid transformation that achieves the best coincidence between them. This procedure is also used to register nearly rigid structures, such as brain structures in neurosurgery, for which adhesive fiducials are placed on the patient's forehead.[9]

Although effective and accurate, contact-based rigid registration methods have two main drawbacks: they require part of the anatomy of interest to be exposed, and they can be time-consuming and error-prone. Intraoperative exposure of all or part of the anatomy of interest to enable it to be touched with a pointer can result in additional undesired surgical incisions. In percutaneous procedures, such as needle insertion or long bone closed fracture reduction, the additional surgical incisions defeat the purpose of the minimally invasive procedure. Additional incisions may also be necessary in some more invasive procedures, such as pelvic fracture reduction, to obtain the desired accuracy with an even distribution of points on the anatomical structure. It is only practical to acquire a few dozen points, because each acquisition is time-consuming. Additional errors are also introduced due to the presence of tissue and fat on the anatomical surface.

An alternative to contact-based registration is image-based registration. In image-based registration, one or more intraoperative images of the anatomy of interest are acquired at known camera poses. Feature points, such as fiducial centers, anatomical landmarks, or anatomical contours, are extracted from the images, and their spatial locations are computed from the camera pose and internal parameters. The most commonly used intraoperative imaging devices are mobile fluoroscopic X-ray C-arms and ultrasound units. The advantage of image-based registration is that it does not require contact or additional surgical exposure, and uses readily available intraoperative imaging devices. It has the potential to be faster and more stable than contact-based registration, because many points can be extracted accurately and automatically with advanced image-processing techniques. However, image-based registration is technically much more challenging, because it depends on many more factors than contact-based registration. These factors include the geometric characteristics of the imaging camera and its pose, the image quality, and the quality of feature localization in the images.

This study establishes a technical framework for comparing the accuracy of both contact-based and image-based landmark registration methods.[10,11] Specifically, we focus on registration using an optical tracker and fluoroscopic X-ray images obtained by common mobile intraoperative C-arm units. To this end, we developed phantoms, protocols, and algorithms for tool tip calibration, contact-based registration, fluoroscopic X-ray camera distortion correction and calibration, and fluoroscopic X-ray image-based landmark registration. We designed and conducted *in vitro* experiments to test the accuracy and reliability of algorithms and protocols under optimal conditions. The individual steps of the registration algorithms were evaluated independently and lower bounds were established.

Previous Work

This section reviews previous work on contact and image-based rigid registration methods, and theoretical and experimental accuracy studies.

Contact-based registration methods are currently in use in many commercial systems. These methods match the actual location of implanted fiducials, anatomical landmarks, or points on the surface of the anatomy (a cloud of points) to the corresponding points in the preoperative model.

The rigid transformation for fiducial and landmark-based registration is obtained directly with Horn's closed form solution,[12] or iteratively by distance minimization.[13] Cloud-of-points registration is performed with the Iterative Closest Point (ICP) method.[14] Several studies have reported millimetric accuracy in clinical settings for contact-based registration.[6,15–19,21]

Several image-based registration methods have been proposed recently, although no commercial system, with the exception of the CyberKnife™ system for radiation therapy of brain tumors,[20] uses them. The registration can be based on geometric features in the image[22–26] or on pixel intensity values.[27–32] Geometric registration requires feature segmentation (e.g., fiducial center location or contour edge detection), while intensity-based registration requires generation of digitally reconstructed radiographic images and their comparison with the actual fluoroscopic X-ray images. The main difficulty with geometric registration is the accuracy and robustness of feature segmentation. The main difficulty with intensity-based registration is the size of the search space and the existence of many local minima. Several groups have reported millimetric accuracy for image-based registration: Lavallée and Hamadeh[23,25] reported an *in vitro* accuracy of 2 mm on a dry vertebra; Tang[26] reported an *in vitro* accuracy of 3 mm on long-bone foam models with six metal fiducials and a single image; and Larose[27] reported an *in vitro* accuracy of 1.3 mm on a $60 \times 60 \times 60\text{-mm}^3$ phantom.

A necessary first step for image-based registration is to obtain an accurate model of the imaging process. The camera has to be calibrated and the image corrected for distortion. Much recent work, including our own,[10,33] has been devoted to fluoroscopic X-ray image distortion correction[2,26,34,35] and pinhole camera calibration.[36,37]

Several theoretical studies on the accuracy of rigid registration have been conducted. Fitzpatrick and West[38–40] analyzed the target registration error (TRE), which is defined as the error between the measured and expected position of a point after registration as a function of the fiducial localization error. They showed that the target registration error does not depend on the initial displacement between the model and the samples, and characterized the dependency of this error's distribution on the spatial configuration of the landmarks or fiducials. Pennec and Thirion[41] presented a statistical framework for point-based registration where geometric features are described as couples, data (coordinates), and uncertainty (covariance matrix). They described a rigid registration algorithm that yields both the motion and its uncertainty and allows the computation of the expected error at every object point. Ellis et al.[42] presented a framework for registration stability evaluation, given known localization error bounds in the registered modalities.

MATERIALS AND METHODS

Algorithms

The goal of our study was to establish a common framework that would allow direct comparison of contact and image-based landmark registration methods. This section presents the generic registration algorithm and a brief review of the algorithms that were used in our study (for full details, see ref. 11).

The registration process consists of five steps:

1. *Calibration*: Calibrate the data acquisition devices (optical tracker, fluoroscopic X-ray C-arm) and correct for distortions.
2. *Feature extraction*: Find features in both data sets, such that a feature in one set can be matched with a corresponding feature in the other.
3. *Feature pairing*: Match the corresponding features in both data sets. Eliminate outlier pairings.
4. *Similarity formulation*: Define a disparity function, which is a global similarity measure between the two data sets, based on the pairings.
5. *Dissimilarity reduction*: Reduce the dissimilarity between the two data sets by minimizing the disparity function.

Steps 2–5 are repeated until convergence is reached.

Contact-Based Registration Method

Contact-based registration consists of matching two 3D point sets. Because the point sets are given, no feature extraction is necessary. When using fiducials or landmarks, the pairing is known since it is determined *a priori* from the point acquisition protocol. The similarity measure between the data sets is the sum of the squared distances between pairs of points in both data sets. We use Horn's closed form solution[12] for point-based registration, and the Iterative Closest Point (ICP) method[14] for cloud-of-points registration. Each sample point is iteratively matched with its nearest neighbor in the model set, and a transformation that minimizes the

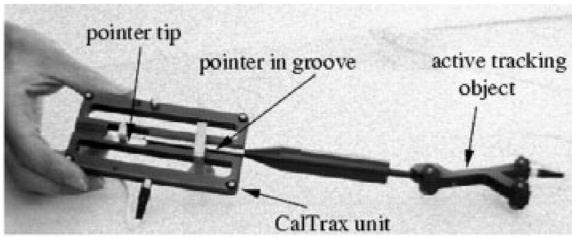

Fig. 1. Photograph of the CalTrax™ unit calibrating an active pointer.

distance between them is then computed using Horn's formula. The algorithm is guaranteed to reach a local minimum, which is also the right one when the initial pose estimate is close enough (e.g., one obtained by approximate landmark).

For contact-based registration, the optical tracker and tool must be calibrated. The tracker does not require calibration because it comes precalibrated from the factory. We calibrate the tool to determine the exact position of the tool tip using a custom calibration algorithm based on the CalTrax™ calibration tool (Traxtal Technologies, Toronto, Canada) shown in Figure 1. The algorithm derives the position of the tool tip from the geometry and position of the tracked pointer and the calibration tool. The geometry is determined by the diameter of the tool and the geometric characteristics of the calibration tool.

Image-Based Landmark Registration Method

Image-based landmark registration consists of matching a set of 3D points (the model) with a set of 2D points extracted from the images—in this case, fiducials.

A prerequisite for fluoroscopic X-ray image-based registration is image distortion correction and calibration, for which we use the algorithms described in ref. 33. The fluoroscopic X-ray C-arm is modeled as a pinhole camera, as this has been shown to be a very good approximation of the X-ray imaging process. We use local bi-linear interpolation on a dense grid of points to compute a distortion map. For camera calibration, we use the pinhole camera calibration algorithm based on constrained optimization, as described by Faugeras.[36] This computes the internal camera parameters (focal length, image center, and scaling) and the external parameters corresponding to the camera pose. The algorithm is more robust and reliable than Tsai's method,[37] which we used originally, although it is very sensitive to small differences in fiducial centers.

Because we perform image-based landmark registration with a phantom consisting of spherical metal balls as fiducials, the feature extraction and feature pairing steps are straightforward. To extract the fiducial centers to subpixel accuracy, we use the circle center Hough transform,[43] followed by gray-level thresholding segmentation. The pairing between the model and computed center is then done manually. We minimize the error measure consisting of the sum of distances between the model points and the closest points on the rays emanating from the camera source and passing through the image points.

Equipment

The equipment used in the study consisted of a standard PC computer with a video card and a monitor, a Phillips BV 29 mobile fluoroscopic X-ray (C-arm) unit with a 9″ field of view (Phillips, Amsterdam, The Netherlands), a hybrid optical tracker (Polaris™, Northern Digital Inc., Ontario, Canada), and tracking instruments from Traxtal Technologies (Toronto, Canada). We used both flat active tracking plates and crosslike optical passive trackers as dynamic reference frames, actively and passively tracked pointers for landmark acquisition, and the CalTrax calibration device for pointer tip calibration (Fig. 1). Images are directly downloaded from the fluoroscopic unit to the PC computer via the video output port with the GrabIt Pro II™ analog-to-digital frame grabber.

Phantoms

We designed and built four custom phantoms for the *in vitro* registration experiments: a dewarp grid, a camera calibration phantom, a contact-based registration phantom, and a four-way registration phantom. With the exception of the dewarp grid, all phantoms have attached to them an active tracking plate that serves as a dynamic reference frame. The holes in the phantoms, which are used as precise landmarks for contact-based registration, are cone shaped, so that the center of a spherical tip pointer inside the hole is invariant with respect to the pointer's orientation.

The dewarp grid is used to correct the images for geometric distortion (Fig. 2). It is a 7-mm-thick coated aluminum alloy plate with 405 4-mm-diameter holes uniformly distributed on a grid at 10-mm intervals machined to 0.02-mm precision. It attaches to the C-arm image intensifier via existing screw holes. This grid is simpler and cheaper to make than the commonly used steel balls or cross hairs mounted on a radiolucent plate. The grid

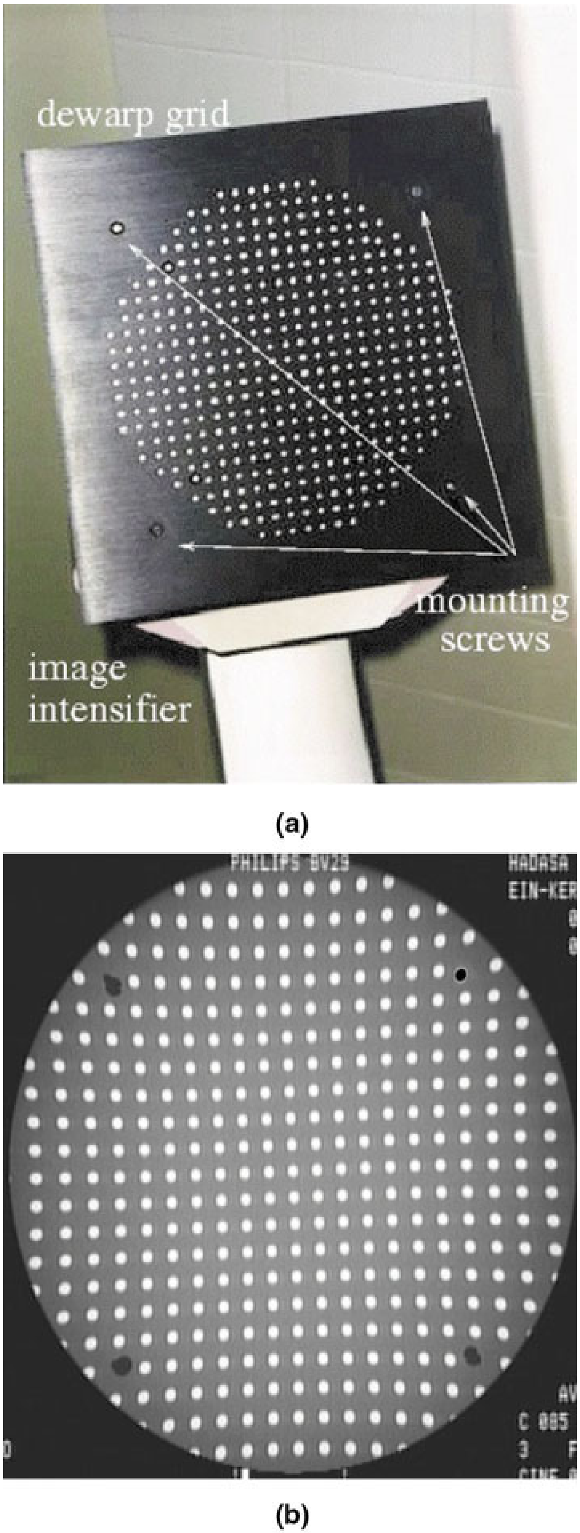

Fig. 2. Dewarp grid on the C-arm image intensifier: (a) photograph, and (b) fluoroscopic image. [Color figure can be viewed in the online issue, which is available at www.interscience.wiley.com]

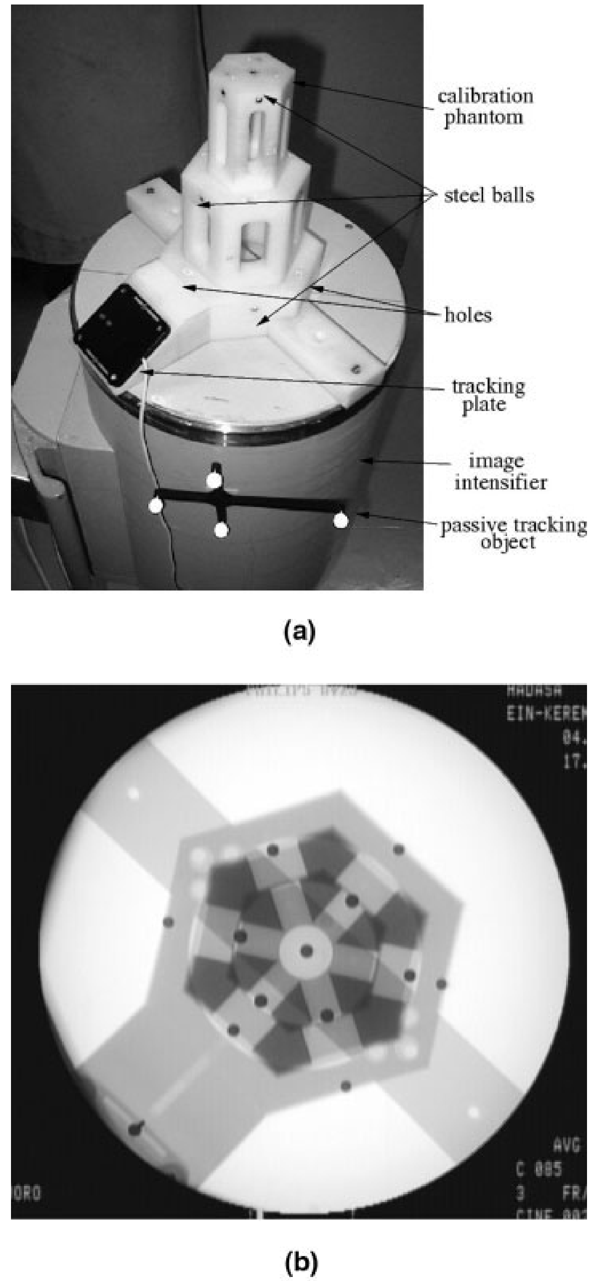

Fig. 3. Camera calibration tower on the C-arm image intensifier: (a) photograph, and (b) fluoroscopic image.

features are sufficiently dense and yield very accurate results.[44]

The camera calibration phantom is used to obtain the intrinsic imaging parameters of the fluoroscopic X-ray unit (Fig. 3). It is a radiolucent, three-step hexagonal tower, with 13 positional holes drilled into it and 12 steel balls pressed into it with a positional accuracy of ± 0.05 mm. The tower dimensions are 200 mm in height and 60 mm, 100

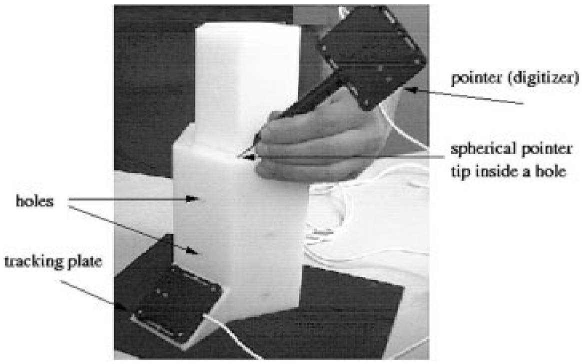

Fig. 4. Photograph of the contact registration phantom with a pointer touching one of the holes on its side.

mm, and 140 mm in external diameter for the upper, middle, and lower steps, respectively. The tower is hollow, with cutout windows on the faces of the middle and upper steps to reduce its weight and increase its radiolucency. It is made out of Delrin™, weighs approximately 1.5 kg, and attaches to the C-arm image intensifier via existing screw holes.

The camera calibration phantom was designed to have three reference planes, and to allow for robust and accurate ball-center computation. The holes are used for contact-based landmark registration to determine the positions of the steel balls during the calibration. The steel balls were placed right above the cutout windows, so that their appearance is sharp and contrasted in the fluoroscopic images. The placement pattern of the holes and balls was designed to avoid radial and mirror symmetry, thus allowing unambiguous automatic pairing. Reducing the weight was important to minimize the C-arm deflection. To verify that our phantom did indeed not affect the C-arm deflection, we attached tracking units to the source and image intensifier and measured their relative position with and without the phantom in several C-arm orientations. No significant difference was detected between measurements with and without the phantom.

The contact-based registration phantom is used for landmark and cloud-of-points contact registration (Fig. 4). It is a two-step hexagonal tower with 31 positional holes whose depth has been measured with a precision of ±0.05 mm. The tower dimensions are 250 mm in height and 70 mm and 100 mm in external diameter for the upper and lower levels, respectively. The tower is a solid piece of Delrin whose dimensions are made to ±0.025-mm accuracy. The holes in the phantom are distributed so as to maximize the number of different distances between them. The surfaces of the object can be used to obtain sampled points from several planes for cloud-of-points contact registration.

The four-way registration phantom can be used for both contact-based landmark and cloud-of-points contact registration, and for landmark image-based and contour image-based registration (Fig. 5). It is an L-shaped base with small L-shaped blocks on top. It has 11 steel balls pressed into it, and nine positional holes drilled into it with a positional accuracy of ±0.05 mm. The L-shaped base has a length of 85 mm, a width of 70 mm, and a height of 40 mm, and the small blocks glued to it are $15 \times 15 \times 15$ mm^3. The phantom is made out of Delrin, and was designed to fit in its entirety in the fluoroscopic image.

The holes in the phantom are arranged so as to allow easy identification and to maximize the distances between them. The steel balls are spatially distributed so as to avoid overlaps from a wide range of viewing directions. The surfaces of the object can be used to obtain sampled points from several planes for cloud-of-points contact registration. The object shape can also be used for contour-based registration, which is not described in this article.

Protocols

We defined the following protocols for tool-tip calibration, contact-based registration, fluoroscopic camera distortion correction and calibration, and image-based landmark registration.

For tool-tip calibration, we place the cylindrical body of the tracked pointer on the CalTrax™ groove and push it until the spherical tip touches the unit's calibration wall (Fig. 1). From the unit geometry and tool diameter, the tool-tip position is determined directly.

For contact-based landmark registration, we touch the holes with the calibrated pointer and apply Horn's closed form solution.[12] For contact-based cloud-of-points registration, we first obtain an approximate initial guess by touching the holes with the calibrated pointer, adding random error to the measurement, and solving in closed form. We then acquire a set of points on the surface of the phantom and apply iterative optimization to obtain the rigid transformation. These methods are applied to all three phantom objects.

For fluoroscopic X-ray camera calibration, we compute the distortion map and the intrinsic camera parameters at predefined C-arm poses. The

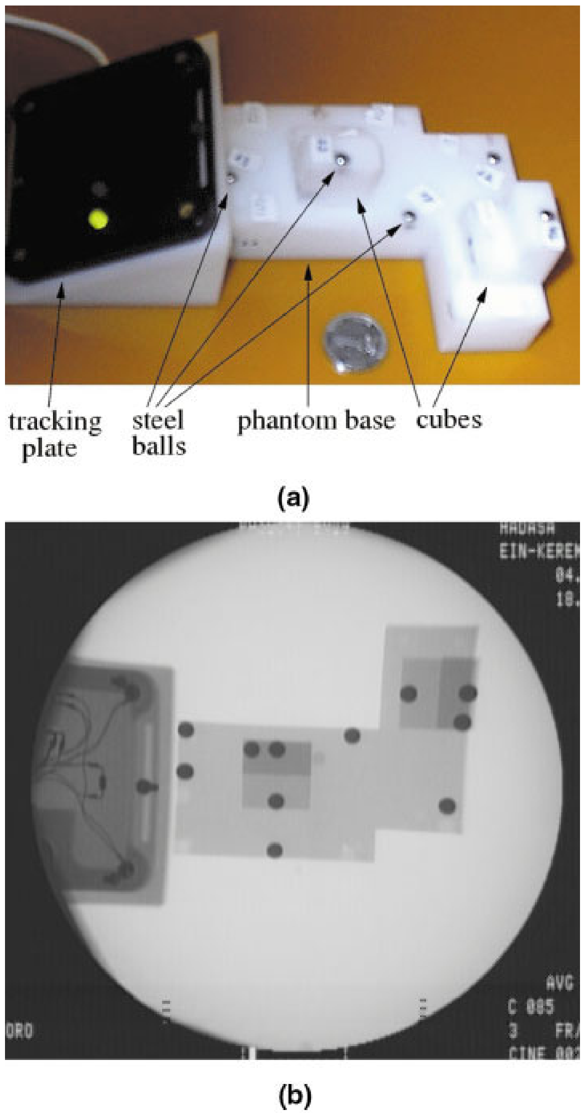

Fig. 5. Four-way registration phantom on a radiolucent table: (a) photograph, and (b) fluoroscopic image acquired from above. [Color figure can be viewed in the online issue, which is available at www.interscience.wiley.com]

images used for calibration are acquired with power settings of 48 and 52 kV, respectively. The image size is 800 × 600 pixels, and the pixel is 0.44 × 0.44 mm^2 after dewarping. To compute the dewarp map, we attach the dewarp grid to the image intensifier, acquire an image, and transfer it to the computer. The plate is then removed, and the calibration phantom is attached in its place. An active tracking plate is fixed on the calibration phantom, and the registration between this plate and the phantom's steel balls is determined using the contact-based landmark registration method. A second tracking plate is attached to the C-arm's image intensifier, and serves as a dynamic reference frame for the C-arm camera. Figure 3 shows the actual setup for calibration. The algorithm then automatically identifies from the fluoroscopic images the centers of the steel balls, whose diameter is 5–10 pixels, to subpixel accuracy, and computes the internal camera parameters using Faugeras' camera calibration method[36] (earlier experiments with Tsai's method[37] were not sufficiently robust). Figure 6 shows the registration chain for the camera calibration protocol.

For image-based landmark registration, we use the four-way calibration object. We place the four-way calibration object on a radiolucent table whose height is roughly level with where a patient lies, and take images from the predetermined poses. After automatically identifying the centers of the steel balls in each image using the same method as above, we manually pair their centers with those of the model and compute the transformation.

RESULTS

We designed and conducted experiments to determine the accuracy of the tracking system, contact-based landmark and cloud-of-points registration,

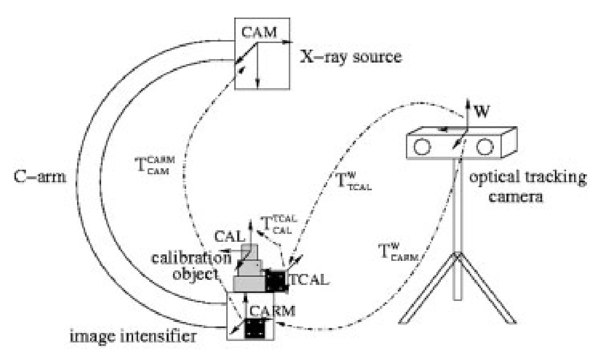

Fig. 6. Schematic view of the C-arm calibration process. The coordinate systems are as follows: *W*, the global coordinate system, which coincides with the tracker's coordinate system; *CARM*, the local coordinate system of the tracking unit attached to the C-arm's image intensifier; *CAL* the local coordinate system of the calibration object; *TCAL*, the local coordinate system of the tracking unit attached to the calibration phantom; and *CAM*, the virtual coordinate system of the camera. The transformations between coordinate systems are: T_{CAM}^{CARM} between the camera and C-arm; T_{CAL}^{TCAL} between the calibration phantom and its tracking plate; T_{TCAL}^{W} between the phantom calibration plate and the world; and T_{CARM}^{W} between the C-arm and the world. The goal is to compute T_{CAM}^{CARM} and the internal camera parameters.

Table 1. Results of Contact-Based Landmark Registration Test (in mm)

No.	Mean	Std dev	Max	Min
(a) Target registration error with five fiducials				
1	0.62	0.25	1.26	0.20
2	0.54	0.22	1.04	0.18
3	0.55	0.23	1.14	0.20
4	0.48	0.17	0.91	0.22
all	0.55	0.22	1.26	0.18
(b) Target registration error with 10 fiducials				
1	0.44	0.23	0.98	0.12
2	0.46	0.21	1.14	0.18
3	0.49	0.34	1.49	0.10
4	0.67	0.33	1.36	0.09
all	0.51	0.29	1.49	0.09

camera calibration, and image-based landmark registration.

Tracking System

To establish a ground-truth basis for the tracker, we estimated the positioning accuracy for a static tool using the Polaris tracking system. The magnitude of this noise defines a limit on the accuracy of all other measurements performed with the system. We placed two calibrated tools on a table and recorded 15,000 samples of their coordinate frames and tool tips. We obtained a deviation of the tools' distance from the tracker's origin in the range of 0.13–0.18 mm, and 0.11–0.21 mm for the tool tips. The larger deviation accounts for the amplification of the tool orientation by the distance along the tools axis. The largest deviation is along the optical axis of the tracker camera.

Contact-Based Landmark Registration Accuracy

The goal of this experiment was to measure the accuracy of the contact-based landmark registration method and to determine if there was a significant improvement when more than five landmark points were used. To this end, we selected five spatially distributed holes on the contact registration phantom, touched them with the pointer to acquire their positions, and computed from them the registration matrix. We then compared the expected position of all 31 holes, including those used for the registration, with the computed ones and averaged the difference to obtain the TRE. We repeated the experiment with ten landmarks, four times each.

Table 1 summarizes the results. We conclude that our tool calibration and fiducial registration algorithm result in submillimetric accuracy, with a mean of 0.55 mm and standard deviation of 0.22 mm with five fiducials, and a mean of 0.51 mm and standard deviation of 0.29 mm with ten fiducials. Note that the improvement with 10 rather than 5 landmarks is relatively small and does not provide a real advantage. This is probably because the results obtained with only five fiducials are already near optimal when considering the error bounds of the tracking system.

Contact-Based Cloud-of-Points Registration Accuracy

The goal of this experiment was to measure the accuracy of the cloud-of-points contact registration and its sensitivity to the initial guess computed from approximate landmarks. We used the same contact-based registration phantom as in the previous section. To simulate the position uncertainty of the landmarks, we added a 2.5-mm error to the hole depth and acquired three landmark positions in different spatial configurations. We used three landmarks for the initial registration and measured its accuracy as described in the previous section. We then acquired a cloud of 15 points on the surface of the phantom, computed the new registration, and compared the results. The experiment was repeated for three different configurations, as shown in Figure 7.

Table 2 summarizes the results. We note that the landmark configuration affects the bias caused by the added error. In the first configuration, two of the landmarks were selected on opposite walls of the hexagon, and the third on the face between them. This caused cancellation of the error, and therefore the initial error was the smallest. In the second configuration, two landmarks on opposite walls were selected, with the third not lying between them. In the third configuration, all landmarks were on the same side of the tower, thereby introducing a bias. As expected, this configuration yielded the worst results. The average error after the cloud-of-points optimization was 1.26 mm, with a standard deviation of 0.68 mm. We conclude that the cloud-of-points registration significantly reduces the error of the initial guess, as expected, but is still dependent on it.

Camera Calibration Accuracy and Sensitivity

The goal of these experiments was to measure the accuracy and sensitivity of the camera calibration process. Prior to the experiments, we calibrated the fluoroscopic camera with the calibration phantom attached to the image intensifier as described above.

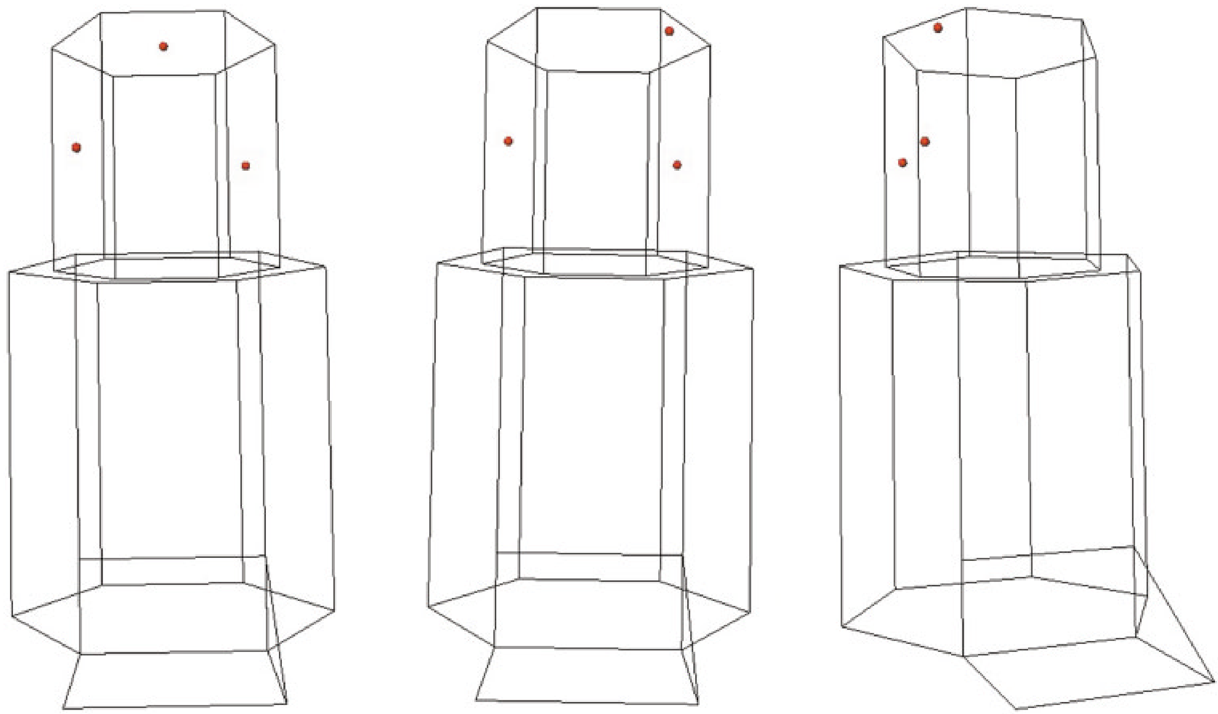

Fig. 7. Three configurations of landmarks for contact-based registration with the contact registration phantom. [Color figure can be viewed in the online issue, which is available at www.interscience.wiley.com]

The first experiment was designed to estimate the calibration accuracy. For this, we used the calibration phantom and imaged it from different angles and at different heights. In the first setup, we placed the calibration phantom on the image intensifier and imaged it at predefined camera angles. In the second setup, we placed the calibration phantom on a radiolucent table and imaged it at a fixed camera angle, but at different heights, by raising and lowering the C-arm. In both cases, we computed the error as the distance between the actual position of the fiducial center (as provided by the tracked position of the phantom and its 3D model) and the back-projected ray emanating from the center of the steel ball in the image to the camera focal point (whose location was known from its tracked position).

Table 2. Results of the Contact Based Registration Experiment
(all errors are in mm)

No.	Mean	Std dev	Max	Min
(a) Coarse registration with three landmarks with 2.5-mm error in hole depth				
1	1.95	1.22	4.43	0.54
2	1.82	0.89	3.58	0.39
3	5.97	3.82	12.93	0.31
all	3.25	3.04	12.93	0.31
(b) Fine registration with a cloud of 15 points and three landmarks with 2.5-mm error				
1	0.86	0.34	1.61	0.33
2	1.60	0.67	3.17	0.50
3	1.31	0.76	2.95	0.24
all	1.26	0.68	3.17	0.24

Table 3 summarizes the results. The first three rows are the results for the calibration phantom on the image intensifier at three different camera angles. The fourth is the result of the calibration phantom on the radiolucent table imaged at different camera heights. The fifth row averages these results. The mean error was 0.84 mm, with a worst case of 2.64 mm. The sixth row shows the residual calibration error computed by taking the same image used for calibration and projecting the ball-centers on it after the calibration parameters were computed. Because this residual error is much smaller than the calibration error (0.15 mm vs. 0.84 mm, on average), it can be neglected.

The second experiment was designed to eval-

Table 3. Results of the First Camera Calibration Accuracy Experiment

Image	Camera angle	Number of fiducials	Mean X shift	Mean Y shift	Mean Z shift	Mean	Std dev	Max	Min
1	0°	31	0.52	−0.04	−0.35	0.67	0.37	1.34	0.08
2	+10°	32	0.21	−0.03	−0.20	0.71	0.35	1.35	0.09
3	−10°	33	0.24	0.00	−0.98	1.12	0.79	2.68	0.14
4	0°	32	0.15	−0.00	−0.42	0.83	0.42	1.77	0.12
1–4	all	128	0.28	−0.02	−0.49	0.84	0.54	2.68	0.08
5	0°	36	0.05	0.00	−0.06	0.15	0.09	0.32	0.02

The first and second columns show the image number and camera angle. Columns 3 to 6 show the average fiducial center shift along each of the three directions relative to the closest point on the ray. The remaining columns show the distances of the fiducials from the closest point on the ray (all values except the C-arm camera angles in the second column are in mm).

uate the sensitivity of the calibration parameters to the fiducial center locations in the image. For each image that was used to compute the calibration parameters, we extracted the fiducial locations with two different gray-level thresholds. This yielded two sets of slightly different fiducial centers, with which two sets of calibration parameters were computed.

Tables 4 and 5 summarize the results. In Table 4, we observe that a variation of 0.23 pixels (0.11 mm) can cause variations of up to 10 mm in some of the projection parameters. However, because the calibration parameters are not independent of each other, a direct comparison of the individual values is not very meaningful. To assess the effect of all the parameters, we computed for the same images the distance between the known fiducial location centers and the back-projected ray for each set of calibration parameters. The results are summarized in Table 5. We note that, despite the fact that the individual parameter changes are large, the mean distance difference is very small (about 0.06 mm).

Image-Based Landmark Registration Accuracy

The goal of this experiment was to quantify the accuracy of image-based landmark registration with the four-way registration phantom. First, we calibrated the fluoroscopic camera as described previously, then took one or more images of the phantom. Using these images, the rigid transformation was computed from the fiducial centers in the image. The accuracy of the resulting transformation was evaluated in two ways. First, the phantom positional holes were used as the target points and the target registration error was measured. Second, we compared the transformation to the "gold standard," which is the transformation obtained by contact-based registration.

Table 6 summarizes the results of the target registration error analysis. We observe that using one AP image produces an error of over 6 mm, most of it along the axis orthogonal to the image plane. This suggests that determining the distance of the registered object along the fluoroscopic cam-

Table 4. Results of the Second Camera Calibration Sensitivity Experiment, Showing the Sensitivity of Computed Camera Parameters to Noise in the Fiducial Detection Algorithm

Image	Mean fiducial centers distance	Focal Distance		Center coordinates	
		Setting 1	Setting 2	Setting 1	Setting 2
1	0.07 (0.16)	969.12	955.80	X = −212.01 Y = −39.79 Z = 1073.25	X = 208.53 Y = 11.58 Z = −1063.49
2	0.06 (0.14)	963.73	953.03	X = 190.92 Y = 28.54 Z = −1074.14	X = −197.16 Y = −37.69 Z = 1063.83
3	0.10 (0.23)	964.02	951.12	X = 192.33 Y = 31.62 Z = −1074.06	X = 171.30 Y = 40.11 Z = −1066.53

The first column is the image number. The second column shows the average distance in mm (pixels in parenthesis) between the detected fiducial on each image in two different settings. The next two columns show the computed camera focal distance (in mm) for each setting. The last two columns show the coordinates (in mm) of the projection center relative to the tracking unit on the C-arm.

Table 5. Results of the Second Camera Calibration Sensitivity Test Showing the Actual Effect of the Change in Camera Parameters on the Back-Projection Process (all values are in mm)

Image #	No. of fiducials	Mean X	Mean Y	Mean Z	Mean
1	12	0.01	<0.01	< 0.01	0.05
2	12	< 0.01	<0.01	0.04	0.05
3	11	0.03	<0.01	0.02	0.06

The X, Y, and Z values denote the differences between the closest points in the back-projection process. The last column displays the mean distance between the closest points.

era's optical axis is the most difficult part of image-based registration. Note that, despite the failure when using the lateral fluoroscopic image of the phantom for registration, combining the data from both camera angles using the least-squares formulation[25] succeeded and improved the registration results significantly. Nevertheless, the overall results of the image-based registration were still poor compared to those obtained with contact-based methods, with an average distance error of 2.75 mm, and 3.4 mm in the worst case when using images from two angles.

Table 7 summarizes the results of the comparison to the gold standard. We observe that the rotation difference is less than 1.5° around each axis in most cases, and about 1° around each axis in the average case. This difference causes errors of about 2 mm when the radius of rotation is 100 mm. Note that larger differences appear in the translational part of the transformation, and that these differences are usually reduced when more images are used as input for the registration procedure. This suggests that the error in the calibration results is related more to the position of the radiation source than to the orientation of the image plane.

DISCUSSION

The goal of our experiments was to establish a framework for comparing the accuracy of contact and image-based landmark rigid registration. For this purpose, we developed phantoms and protocols for testing algorithms for tool tip calibration, contact-based registration with an optical tracker, fluoroscopic X-ray camera calibration, and fluoroscopic X-ray image-based landmark registration.

All the experiments were conducted under optimal laboratory conditions, which are not necessarily those of the operating room. The goal was to establish a lower bound on the system accuracy and to identify and quantify the weak links of the registration framework. Understanding of the factors that affect the accuracy and robustness of the registration process provides quantitative criteria to support the selection of registration methods, and indicates where technical improvements are necessary.

We found an average accuracy of 0.5 mm (1.5 mm maximum) and 2.75 mm (3.4 mm maximum) for contact-based and image-based landmark registration, respectively. We also found that, for contact-based registration, five fiducials are enough to produce near-optimal results, most likely due to the accuracy of the tracking systems. Although the accuracy of contact-based landmark registration is close to the accuracy of the tracking system, the accuracy decreases with cloud-of-points and image-based landmark registration. We identified the fluoroscopic X-ray camera calibration process as being the main source of error in image-based registration. This is because the projection parameters computed for one fluoroscopic image do not accurately fit the projection of other images taken while the fluoroscope's position remains fixed. Despite the errors in our experimental results, we have shown that our protocols can be used to compute

Table 6. Results of the Image-Based Landmark Registration Test

Registration	Mean Shift			Std shift			Distance			
base	X	Y	Z	X	Y	Z	mean	std	max	min
Contact	0.18	0.27	−0.14	0.10	0.10	0.08	0.38	0.05	0.46	0.31
AP	1.72	−1.09	−6.06	0.41	0.24	0.11	6.41	0.08	6.51	6.29
Lateral					-Failed-					
AP + lateral	1.68	−1.51	1.51	0.45	0.36	0.11	2.75	0.47	3.37	2.16

Three computations of image-based registration were made, two of them based on a single image (anterior/posterior (AP) and lateral) and one on both. Columns 2–4 show the mean shift of the phantom positional holes relative to the hole position computed from the registration matrix. Columns 5–7 show the standard deviation of this shift. Columns 8–11 show the mean, standard deviation, maximum, and minimum distance between these points (all values are in mm).

Table 7. Results of the Comparison between Contact and Image Based Landmark Registration Tests

Data Set/Number	Rotation variation			Translation variation		
of Images	X	Y	Z	X	Y	Z
Series 1						
One image	0.55	−0.23	1.05	−5.87	2.42	1.60
Two images	1.11	0.10	1.57	−1.19	−0.23	1.66
Three images	2.06	0.41	2.23	1.43	−2.22	1.45
Mean	1.24	0.09	1.62	−1.88	−0.01	1.57
Series 2						
One image	0.08	0.21	0.67	−4.60	−4.15	1.72
Two images	0.07	0.21	0.72	2.31	−0.66	1.60
Mean	0.07	0.21	0.69	−1.14	−2.40	1.66
Relative values mean	0.77	0.14	1.25	−1.58	−0.97	1.61
Absolute values mean	0.77	0.23	1.25	3.08	1.94	1.61

The values are the difference between the transformation matrix rotation and translation parameters obtained with image-based landmark registration and those obtained with contact-based landmark registration (rotation values are in degrees, translation values are in mm).

rigid registration with a millimetric accuracy under optimal conditions.

CONCLUSION AND FUTURE WORK

We have described a methodology and an *in vitro* study of two types of rigid registration methods for computer-aided surgery: contact-based and image-based landmark registration. We have described phantoms, protocols, and algorithms for tool tip calibration, contact-based registration with an optical tracker, fluoroscopic X-ray camera calibration, and fluoroscopic X-ray image-based landmark registration. Camera calibration was identified as the main source of error in image-based registration. These results indicate that, in contrast to contact-based registration, image-based landmark registration requires further improvement before it can be used clinically.

Because camera calibration was identified as the single most important factor of error in image-based registration, a new calibration and tracking ring for the C-arm was designed and built, and the calibration algorithm has been improved.[45] Preliminary studies show a twofold improvement in the accuracy, demonstrating that image-based registration has potential for clinical use. We are currently developing registration algorithms for contour-based registration, which are being validated with dry bones. Plans for future work include *in vivo* studies.

ACKNOWLEDGMENT

This research was supported in part by a grant from the Israel Ministry of Industry and Trade for the IZMEL Consortium on Image-Guided Therapy. We thank Neil Glossop from Traxtal Technologies for his advise and support.

REFERENCES

1. DiGioia AM, Simon DA, Jaramaz B, Blackwell M, Morgan F, O'Toole RV, Colgan B. HipNav: Preoperative planning and intraoperative navigational guidance for acetabular implant placement in total hip replacement surgery. In: Nolte LP, Ganz R, editors: Computer Assisted Orthopedic Surgery. Bern, Switzerland: Hogrefe and Huber Publishers, 1999.
2. Hofstetter R, Slomczykowski M, Sati M, Nolte LP. Fluoroscopy as an imaging means for computer assisted surgical navigation. Comp Aid Surg 1999;4(2):65–76.
3. Taylor RH, Lavallée S, Burdea G, Mösges R, editors: Computer-Integrated Surgery: Technology and Clinical Applications. Cambridge, MA: MIT Press, 1996.
4. Joskowicz L, Milgrom C, Simkin A, Tockus L, Yaniv Z. FRACAS: A system for computer-aided image-guided long bone fracture surgery. Comp Aid Surg 1998;3(6):271–288.
5. Zamorano L, Matter A, Saenz A, Buciuc R, Diaz F. Interactive image-guided resection of cerebral cavernous malformations. Comp Aid Surg 1997;2(6):327–332.
6. Smith K, Frank KJ, Bucholz R. The Neurostation: a highly accurate, minimally invasive solution to frameless stereotactic neurosurgery. Comp Med Imag Graphics 1994;18(1):247–256.
7. Hassfeld S, Mühling J. Navigation in maxillofacial and craniofacial surgery. Comp Aid Surg 1998;3(1):183–187.
8. Maintz JBA, Viergever MA. A survey of medical image registration. Med Image Anal 1998;2(1):1–36.
9. Darabi K, Grunert P, Perneczky A. Accuracy of intraoperative navigation using skin markers. In: Lemke HU, Vannier MW, Inamura K, editors: Computer Assisted Radiology and Surgery. Proceedings of the 11th International Symposium and Exhibition (CAR'97), Berlin, June 1997. Amsterdam: Elsevier, 1997. p 920–924.
10. Yaniv Z, Sadowsky O, Joskowicz L. In-vitro accuracy

study of contact and image-based registration: materials, methods, and experimental results. In: Lemke HU, Vannier MW, Inamura K, Farman AG, Doi K, editors: Computer Assisted Radiology and Surgery. Proceedings of the 14th International Congress and Exhibition (CARS 2000), San Francisco, 28 June–1 July 2000. Amsterdam: Elsevier, 2000. p 141–146.

11. Sadowsky O. Contact and image-based rigid registration in computer-assisted surgery: materials, methods, and experimental results. Master's thesis, School of Computer Science and Engineering, The Hebrew University of Jerusalem, 2001.
12. Horn BKP. Closed-form solution of absolute orientation using unit quaternions. J Optical Soc Am A 1987;4(4):629–642.
13. Lavallée S. Registration for computer-integrated surgery: methodology, state of the art. In: Taylor RH, Lavallée S, Burdea G, Mösges R, editors: Computer-Integrated Surgery: Technology and Clinical Applications. Cambridge, MA: MIT Press, 1996. p 77–97.
14. Besl PJ, McKay ND. A method for registration of 3D shapes. IEEE Trans Pattern Anal Machine Intell 1992; 14(2):239–255.
15. Bolger C, Wigfield C, Melkent T, Smith K. Frameless stereotaxy and anterior cervical surgery. Comp Aid Surg 1999;4(6):322–327.
16. Gong J, Bächler R, Sati M, Nolte LP. Restricted surface matching, a new approach to registration in computer assisted surgery. In: Troccaz J, Grimson E, Mösges R, editors: Proceedings of First Joint Conference on Computer Vision, Virtual Reality and Robotics in Medicine and Medical Robotics and Computer Assisted Surgery (CVRMed-MRCAS'97), Grenoble, France, March 1997. Lecture Notes in Computer Science 1205. Berlin: Springer, 1997. p 597–605.
17. Germano IM, Queenan JV. Clinical experience with intracranial brain needle biopsy using frameless surgical navigation. Comp Aid Surg 1998;3(1):33–39.
18. Schmerber S, Chassat F. Accuracy evaluation of a CAS system: laboratory protocol and results with 6D localizers, and clinical experiences in otorhinolaryngology. Comp Aid Surg 2001;13(1):1–6.
19. Simon DA, Jaramaz B, Blackwell M, Morgan F, DiGioia AM, Kischell E, Colgan B, Kanade T. Development and validation of a navigational guidance system for acetabular implant placement. In: Troccaz J, Grimson E, Mösges R, editors: Proceedings of First Joint Conference on Computer Vision, Virtual Reality and Robotics in Medicine and Medical Robotics and Computer Assisted Surgery (CVRMed-MRCAS'97), Grenoble, France, March 1997. Lecture Notes in Computer Science 1205. Berlin: Springer, 1997. p 583–592.
20. Adler JR, Murphy MJ, Chang SD, Hancock SL. Image-guided robotic radiosurgery. Neurosurgery 1999; 44(6):1299–1307.
21. Villalobos H, Germano IM. Clinical evaluation of multimodality registration in frameless stereotaxy. Comp Aid Surg 1999;4(1):45–49.
22. Guéziec A, Kazanzides P, Williamson B, Taylor RH. Anatomy based registration of CT-scan and intraoperative X-ray images for guiding a surgical robot. IEEE Trans Med Imaging 1998;17(5):715–728.
23. Hamadeh A, Lavallée S, Cinquin P. Automated 3-dimensional computed tomographic and fluoroscopic image registration. Comp Aid Surg 1998;3(1):11–19.
24. Hamadeh A, Sautot P, Lavallée S, Cinquin P. Towards automatic registration between CT and X-ray images: cooperation between 3D/2D registration and 2D edge detection. Proceedings of Second Annual Symposium on Medical Robotics and Computer Assisted Surgery, Baltimore, Maryland, November 1995. New York: Wiley, 1995. p 39–46.
25. Lavallée S, Szeliski R, Brunie L. Anatomy-based registration of 3D medical images, X-ray projections, and 3D models using octree-splines. In: Taylor RH, Lavallée S, Burdea G, Mösges R, editors: Computer-Integrated Surgery: Technology and Clinical Applications. Cambridge, MA: MIT Press, 1996. p 115–143.
26. Tang TSY. Calibration and point based registration of fluoroscopic images. Master's thesis, Department of Computing and Information Science, Queen's University, Kingston, Ontario, Canada, 1999.
27. LaRose D. Iterative X-ray/CT registration using accelerated volume rendering. PhD thesis, Robotics Institute, Carnegie Mellon University, Pittsburgh, PA, May 2001.
28. Lemieux L, Jagoe R, Fish DR, Kitchen ND, Thomas GT. A patient-to-computed-tomography image registration method based on digitally reconstructed radiographs. Med Phys 1994;21(11):1749–1760.
29. Murphy MJ. An automatic six-degree-of-freedom registration algorithm for image-guided frameless stereotaxic radiosurgery. Med Phys 1997;24(6):857–866.
30. Penney GP, Weese J, Little JA, et al. A comparison of similarity measures for use in 2D-3D medical image registration. IEEE Trans Med Imaging 1998;17:586–595.
31. Roth M, Brack C, Burgkart R, Czopf A, Götte H, Schweikard A. Multi-view contourless registration of bone structures using a single calibrated X-ray fluoroscope. In: Lemke HU, Vannier MW, Inamura K, Farman AG, editors: Computer Assisted Radiology and Surgery. Proceedings of the 13th International Congress and Exhibition (CARS'99), Paris, France, June 1999. Amsterdam: Elsevier, 1999. p 756–761.
32. Pluim JPW, Maintz JBA, Viergever MA. Image registration by maximization of combined mutual information and gradient information. In: Delp SL, DiGioia AM, Jaramaz B, editors: Proceedings of Third International Conference on Medical Image Computing and Computer-Assisted Intervention (MICCAI 2000), Pittsburgh, PA, October 2000. Lecture Notes in Computer Science 1935. Berlin: Springer, 2000. p 452–461.

33. Yaniv Z. Fluoroscopic X-ray image processing and registration for computer-aided orthopedic surgery. Master's thesis, Institute of Computer Science, The Hebrew University of Jerusalem, 1998.
34. Brack C, Burgkart R, Czopf A, Götte H, Roth M, Radig B, Schweikard A. Accurate X-ray-based navigation in computer-assisted orthopedic surgery. In: Lemke HU, Vannier MW, Inamura K, Farman AG, editor: Computer Assisted Radiology and Surgery. Proceedings of the 12th International Symposium and Exhibition (CAR'98). Amsterdam: Elsevier, 1998. p 716–722.
35. Schreiner S, Funda J, Barnes AC, Anderson JH. Accuracy assessment of a clinical biplane fluoroscope for three-dimensional measurements and targeting. In: Proceedings of SPIE Medical Imaging, 1995.
36. Faugeras O. Three-Dimensional Computer Vision: A Geometric Viewpoint. Cambridge, MA: MIT Press, 1993.
37. Tsai R. A versatile camera calibration technique for high-accuracy 3D machine vision metrology using off-the-shelf TV cameras and lenses. IEEE Trans Robotics Automat 1987;RA-3(4):323–344.
38. Fitzpatrick JM, West JB, Maurer CR Jr. Predicting error in rigid-body, point-based registration. IEEE Trans Med Imaging 1998;17(5):694–702.
39. Fitzpatrick JM, West JB. The distribution of target registration error in rigid-body, point-based registration. IEEE Trans Med Imaging 2001;20:917–927.
40. West JB. Predicting error in point-based registration. PhD thesis, Department of Computer Science, Vanderbilt University, Nashville, Tennessee, 2000.
41. Pennec X, Thirion JP. A framework for uncertainty and validation of 3D registration methods based on points and frames. Int J Comp Vision 1997;25(1):203–229.
42. Ellis RE, Fleet DJ, Bryant JT, Rudan J, Fenton P. A method for evaluating CT-based surgical registration. In: Troccaz J, Grimson E, Mösges R, editors: Proceedings of First Joint Conference on Computer Vision, Virtual Reality and Robotics in Medicine and Medical Robotics and Computer Assisted Surgery (CVRMed-MRCAS'97), Grenoble, France, March 1997. Lecture Notes in Computer Science 1205. Berlin: Springer, 1997. p 141–150.
43. Leavers VF. Which Hough transform? Comput Vision Graphics Image Process Image Understand 1993;58(2):250–264.
44. Yaniv Z, Joskowicz L, Simkin A, Garza-Jinich M, Milgrom C. Fluoroscopic image processing for computer-aided orthopaedic surgery. In: Wells WM, Colchester A, Delp S, editors: Proceedings of First International Conference on Medical Image Computing and Computer-Assisted Intervention (MICCAI'98), Cambridge, MA, October 1998. Lecture Notes in Computer Science 1496. Berlin: Springer, 1998. p 325–334
45. Livyatan H, Yaniv Z, Joskowicz L. Robust automatic C-arm calibration for fluoroscopy-based navigation: a practical approach. In: Dohi T, Kikinis R, editors: Proceedings of the 5th International Conference on Medical Image Computing and Computer-Aided Intervention (MICCAI′ 2002) Tokyo, Japan, October 2002. Lecture Notes in Computer Science, 2488. Berlin: Springer, 2002. Vol 2. p 60–68.